J. Fluid Mech. (2010), *vol.* 664, *pp.* 313–336. © Cambridge University Press 2010
doi:10.1017/S002211201000385X

Evolution of weakly nonlinear random directional waves: laboratory experiments and numerical simulations

A. TOFFOLI[1]†, O. GRAMSTAD[2], K. TRULSEN[2], J. MONBALIU[3], E. BITNER-GREGERSEN[1] AND M. ONORATO[4]

[1]Det Norske Veritas, Veritasveien 1, NO-1322 Høvik, Norway

[2]Department of Mathematics, University of Oslo, PO Box 1053 Blindern, NO-0316 Oslo, Norway

[3]KU Leuven, Kastlepark Arenberg 40, 3001 Heverlee, Belgium

[4]Dipartimento di Fisica Generale, Università di Torino, Via P. Giuria 1, 10125 Torino, Italy

(Received 14 October 2009; revised 13 July 2010; accepted 13 July 2010;
first published online 15 October 2010)

Nonlinear modulational instability of wavepackets is one of the mechanisms responsible for the formation of large-amplitude water waves. Here, mechanically generated waves in a three-dimensional basin and numerical simulations of nonlinear waves have been compared in order to assess the ability of numerical models to describe the evolution of weakly nonlinear waves and predict the probability of occurrence of extreme waves within a variety of random directional wave fields. Numerical simulations have been performed following two different approaches: numerical integration of a modified nonlinear Schrödinger equation and numerical integration of the potential Euler equations based on a higher-order spectral method. Whereas the first makes a narrow-banded approximation (both in frequency and direction), the latter is free from bandwidth constraints. Both models assume weakly nonlinear waves. On the whole, it has been found that the statistical properties of numerically simulated wave fields are in good quantitative agreement with laboratory observations. Moreover, this study shows that the modified nonlinear Schrödinger equation can also provide consistent results outside its narrow-banded domain of validity.

Key words: surface gravity waves

1. Introduction

A proper description of the probability of occurrence of extreme waves is vital for the design and operation of marine structures. Many mechanisms can be responsible for the formation of extreme events such as the wave–current interaction, linear Fourier superposition and nonlinear dispersive focusing and modulational instability (see e.g. Kharif & Pelinovsky 2003; Dysthe, Krogstad & Müller 2008, and references therein for a complete review). In the open ocean, in the absence of strong currents,

† Present address: Faculty of Engineering and Industrial Sciences, Swinburne University of Technology, PO Box 218, Hawthorn, Victoria 3122, Australia. Email address for correspondence: toffoli.alessandro@gmail.com

https://doi.org/10.1017/S002211201000385X Published online by Cambridge University Press

the statistical properties of water waves can be conveniently described by modelling the surface elevation with a second-order expansion in the wave steepness ε of the water wave equations (Longuet-Higgins 1963). Based on this approach a number of second-order probability distributions have been proposed by many authors in the past few decades (see e.g. Tayfun 1980; Arhan & Plaisted 1981; Prevosto, Krogstad & Robin 2000; Forristall 2000; Tayfun & Fedele 2007).

Despite the fact that second-order models agree with field measurements reasonably well (see e.g. Forristall 2000; Toffoli *et al.* 2007), deviations from second-order based statistical distributions are still possible (Bitner-Gregersen & Magnusson 2004; Petrova, Cherneva & Guedes Soares 2006). In this respect, it is important to mention that the second-order approximation can provide an accurate estimate of the skewness of the surface elevation, but it is not in principle adequate to describe the whole probability density function (p.d.f.; see Janssen 2009). Furthermore, a second-order expansion only includes effects related to bound waves, while the nonlinear dynamics of free waves is neglected. To third order in wave steepness, however, wavetrains can be unstable to small perturbations which can cause a local exponential growth in the wave amplitude within a time frame of a few tens of wave periods (Janssen 2003). The mechanism involved is basically a generalization of the Benjamin–Feir instability (Benjamin & Feir 1967) or modulational instability (Zakharov 1968).

At cubic order, the instability of quasi-periodic deep-water wavetrains due to modulational perturbations is governed by the nonlinear Schrödinger equation (NLS equation; Zakharov 1968). This equation can be derived from the Euler equations assuming potential flow of free-surface waves that are weakly nonlinear (i.e. $\varepsilon = ka \ll 1$, where k is the wavenumber and a is the wave amplitude) and have narrow bandwidth ($\Delta k/k \ll 1$, where Δk is a modulation wavenumber). A modification of the NLS equation, which takes into account the fourth order in wave steepness and bandwidth, was derived by Dysthe (1979) on the basis of a systematic asymptotic procedure (this equation is known as the Dysthe equation). It should be kept in mind that the bandwidth constraint seriously limits the application of nonlinear Schrödinger equations for ocean wave fields. Therefore, Trulsen & Dysthe (1996) extended the Dysthe equation with the addition of higher-order dispersive terms allowing the description of slightly broader bandwidths.

Nonlinear Schrödinger equations have received considerable attention by wave researchers primarily due to their simplicity and to their integrability using the inverse scattering transform (Zakharov & Shabat 1972). Moreover, they are not computationally expensive. Thus, numerical models based on such equations are particularly suitable to investigate wave statistics, which requires the calculation of many realizations of a random sea surface (see, for example, Onorato *et al.* 2001; Onorato, Osborne & Serio 2002*a*; Socquet-Juglard *et al.* 2005; Gramstad & Trulsen 2007). In this respect, model results show that the instability of wavepackets and the consequent growth of large-amplitude waves can modify substantially the form of the p.d.f. of the surface elevation. Strong deviations from Gaussian and second-order statistics occur for narrow-banded near-unidirectional wave spectra where most of the energy is confined within a narrow range of frequencies and directions (Onorato *et al.* 2001; Socquet-Juglard *et al.* 2005). As the directional spreading increases to that of more realistic directional wave fields, the deviations from Gaussian wave statistics diminish, rendering a short-crested sea with only weakly non-Gaussian wave statistics. Under these circumstances the p.d.f. of the surface elevation matches second-order

https://doi.org/10.1017/S002211201000385X Published online by Cambridge University Press

predictions (Onorato *et al.* 2002*a*; Socquet-Juglard *et al.* 2005; Gramstad & Trulsen 2007).

The effect of modulational instability on random wave fields, and in particular the transition between strongly and weakly non-Gaussian statistics, were confirmed in a number of wave flume (Onorato *et al.* 2005*b*, 2006) and directional wave tank experiments (Stansberg 1994; Denissenko, Lukaschuk & Nazarenko 2007; Onorato *et al.* 2009*a*,*b*; Waseda, Kinoshita & Tamura 2009). Nonetheless, a direct quantitative comparison between numerical model results and laboratory experiments has not been discussed yet. While discrepancies in deterministic evolution between nonlinear Schrödinger equations and exact models are well documented (see e.g. Clamond *et al.* 2006), our present goal is to assess how well the two selected numerical models capture the statistical properties of directional wave fields.

Because of the narrow bandwidth constraint, the nonlinear Schrödinger equations are not well suited for describing broad-banded sea states. In order to improve the description of a broad-banded sea, one may use a model without bandwidth constraints. One such model is the Zakharov equation, which describes the evolution of weakly nonlinear waves of any bandwidth, and may be used in numerical simulations (see e.g. Annenkov & Shrira 2001). The surface elevation may also be simulated directly from the potential Euler equations. In this respect, there exist a number of methods that allow the simulation of fully nonlinear waves (see, for example, Tsai & Yue 1996; Bateman, Swan & Taylor 2001; Clamond & Grue 2001; Zakharov, Dyachenko & Vasilyev 2002; Fochesato & Dias 2006). These models have been used to investigate the evolution of waves of exceptional wave steepness and height, i.e. rogue or freak waves (e.g. Clamond & Grue 2001; Fochesato, Grilli & Dias 2007). However, they have not been applied to the computation of random directional wave fields over a large spatial domain due to the computational burden. A promising method that allows the prediction of statistical properties of fully nonlinear waves was recently presented by Gibson, Swan & Tromans (2007), who combined the fully nonlinear wave model by Bateman *et al.* (2001) with a spectral response surface method; this study, however, was limited to unidirectional waves. In several studies (see e.g. Tanaka 2001*a*, 2007; Mori & Yasuda 2002; Ducrozet *et al.* 2007; Toffoli *et al.* 2007, 2008*a*, 2009), the simulation of a large number of realizations of the random sea surface was conveniently calculated from truncated Euler equations by using a higher-order spectral method (HOSM), which was derived independently by Dommermuth & Yue (1987) and West *et al.* (1987). Results for directional sea states seem to be consistent with previous simulations of Schrödinger-type equations.

As the observation of extreme waves is rare in nature, model results represent an important source of information for their statistics. Therefore, there is a substantial need for reliable and computationally efficient numerical tools. A quantitative comparison between numerical predictions of the statistical properties of directional wave fields and experimental observations is the main aim of the present study. For this purpose, we make use of a set of observations of mechanically generated short-crested waves with different degrees of directionality which were collected in a directional wave tank (Onorato *et al.* 2009*a*). An estimation of the observed statistical properties is then reconstructed by using two different approaches: (i) the modified nonlinear Schrödinger equation (Trulsen & Dysthe 1996) and (ii) the truncated potential Euler equations solved with an HOSM (Dommermuth & Yue 1987; West *et al.* 1987). We stress that whereas the first is derived for narrow-banded conditions, the latter is free from bandwidth constraints. However, both models assume weak nonlinearity.

https://doi.org/10.1017/S002211201000385X Published online by Cambridge University Press

This paper is organized as follows. In § 2, we briefly describe the laboratory experiments. The descriptions of the numerical models as well as their initial conditions are presented in § 3. It is important to mention that the numerical experiments are carried out respecting the domain of validity of the equations; resolution of the initial conditions is therefore chosen such that both models can perform in their optimal conditions in terms of accuracy and computational time. The differences between the two numerical approaches are discussed. As waves evolve, the spectrum changes its shape with a consequent modification of the initial spectral conditions. An analysis of the spectral changes is presented in § 4; experimental and numerical results are compared. In § 5, a comparative analysis between the statistical properties of observed and simulated directional wave fields is presented; particular attention is given to the transition between strongly and weakly non-Gaussian properties. The study is based on the p.d.f. of the surface elevation and its third- and fourth-order moments (skewness and kurtosis respectively). Effects related to the discreteness of the computational domain are discussed. Concluding remarks are then presented in the last section.

2. Laboratory experiments

Laboratory tests have been performed at the Marintek wave facilities in Trondheim, Norway. A detailed description of the facilities and experiments is presented in an earlier paper (Onorato *et al.* 2009*a*). In the following, we only provide a brief summary.

2.1. *The wave basin*

Directional wave fields have been generated in a large rectangular wave basin with dimensions of 70 m × 50 m. The basin is equipped with a wavemaker along the 70 m side, which consists of altogether 144 individually computer-controlled flaps. This unit can generate short-crested seas within a wide range of directional distributions of the wave energy. The basin is also equipped with a system that is capable of changing the water depth; for the present experiments the water depth was fixed at 3 m.

Wave measurements have been concentrated along the central axis of the basin (see figure 1) to trace the evolution of the wave field as waves propagate from the wavemaker. Wave probes, which are held across the water surface by tripods standing on the bottom, are deployed at 5 m intervals. The temporal profile of the surface elevation is recorded with a sampling frequency of 80 Hz. In this respect, it is important to note that the recorded time series represents the wave field at a fixed stage of development. At locations 5, 25 and 35 m from the wavemaker, two additional probes were deployed to allow the reconstruction of directional wave spectra (figure 1). At 25 m from the wavemaker, moreover, an eight-gauge array, which was arranged as a regular heptagon plus a central probe, was also deployed. A description of the available methods to reconstruct the directional wave spectrum can be found in Young (1994) and Donelan, Drennan & Magnusson (1996). We should mention that an inspection of directional spectra did not show any significant reflection from the sidewalls.

Note that the experiments were carried out in a finite size basin. Therefore, the discreteness of the facility may have affected the result (see, for example, Denissenko *et al.* 2007). Nonetheless, a comparison with experimental results obtained in an independent directional wave tank with different dimensions (Onorato *et al.* 2009*b*) showed that wave statistics are not significantly affected by the aspect ratio of the facility.

https://doi.org/10.1017/S002211201000385X Published online by Cambridge University Press

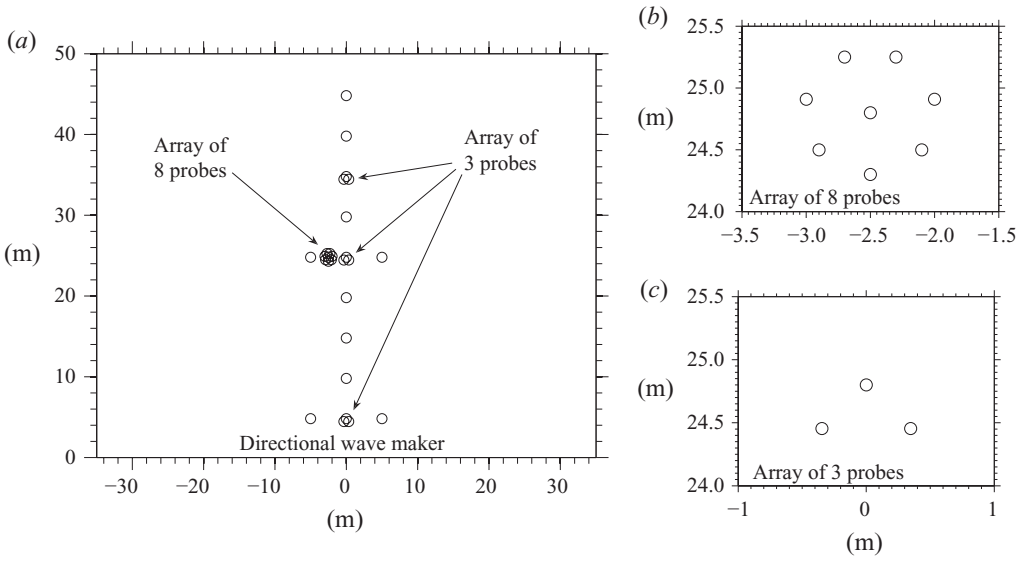


FIGURE 1. (*a–c*) Wave basin and positions of the wave gauges.

2.2. *Conditions at the wave maker*

Series of irregular waves were generated from an input spectrum with 16 384 frequencies distributed between 0.0 and 10.0 Hz. Amplitudes were randomly chosen from the Rayleigh distribution, while the random phases were assumed to be uniformly distributed in the interval [0, 2π). Therefore, an initial Gaussian wave field is here used as input. It is important to mention, however, that in nature deviations from Gaussianity are often present and consequently the wave amplitudes are not Rayleigh-distributed and the phases are not uniformly distributed (see Bitner 1980). Adoption of non-Gaussian initial wave conditions in the experiment and numerical models might lead to different evolution of wave surface. This condition is not investigated in the present study, however.

In order to have enough samples to produce a statistical analysis, four realizations of the random sea surface with the same imposed spectrum were performed by using different sets of random amplitudes and phases. For each test, 20 min of wave records were collected, including the initial ramp-up. For all of the probes, a total of about 3.5×10^5 measures of the surface elevation were gathered. The variability of the statistical properties of the sample can be estimated by using bootstrap methods (see e.g. Emery & Thomson 2001). We observed that whereas this sample ensures a negligible 95 % confidence interval for the third-order moment of the p.d.f. (skewness), i.e. ± 0.01, the fourth-order moment (kurtosis) is subjected to some variability; within the 95 % confidence intervals, the value of the kurtosis may vary within a range of ± 0.12.

Experiments were conducted by imposing different input directional wave spectra $E(\omega, \vartheta) = S(\omega)\, D(\vartheta)$, where $S(\omega)$ represents the frequency spectrum and $D(\vartheta)$ is a frequency-independent directional distribution. The energy distribution in the frequency domain was described by using the Joint North Sea Wave Project (JONSWAP) formulation (see e.g. Komen *et al.* 1994):

$$S(\omega) = \frac{2\pi\alpha g^2}{\omega^5} \exp\left[-\frac{5}{4}\left(\frac{\omega}{\omega_p}\right)^{-4}\right] \gamma\left(\exp\left[-(\omega-\omega_p)^2/\left(2\sigma^2\omega_p^2\right)\right]\right), \qquad (2.1)$$

https://doi.org/10.1017/S002211201000385X Published online by Cambridge University Press

T_p (s)	α	γ	H_s (m)	λ_p (m)	k_p (m^{-1})	k_pa	BFI
1.0	0.014	3.0	0.06	1.56	4.02	0.13	0.70
1.0	0.016	6.0	0.08	1.56	4.02	0.16	1.10

TABLE 1. Parameters for the input JONSWAP spectra.

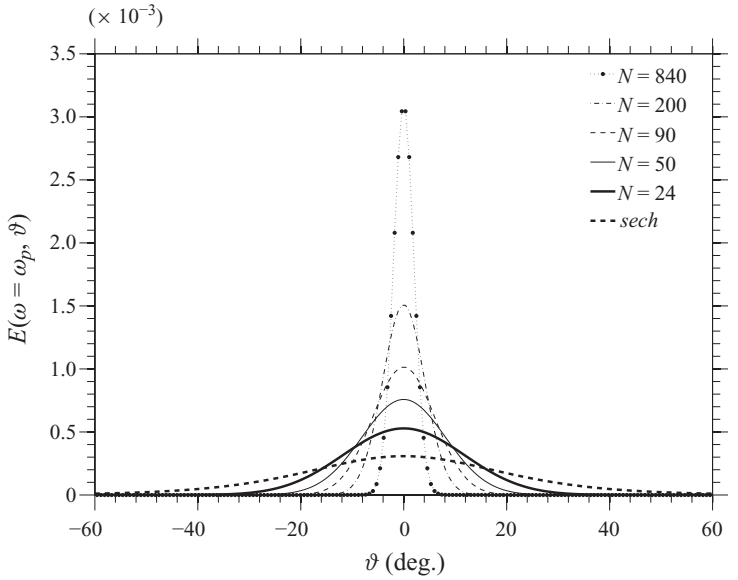


FIGURE 2. Energy directional distribution as a function of the angle ϑ for different values of the parameter N; just for reference, the *sech* parametrization described in Komen *et al.* (1994) is also included.

where ω is the angular frequency and ω_p is the peak frequency; the parameter σ is equal to 0.07 if $\omega \leqslant \omega_p$ and 0.09 if $\omega > \omega_p$. For the present study, we have chosen to describe the wave field with a peak period $T_p = 1$ s, which corresponds to a peak wavelength λ_p of 1.56 m. Two different pairs of the Phillips parameter α and the peak enhancement factor γ have then been chosen. This implies different values of the wave steepness $\varepsilon = k_pa$, where $k_p = 2\pi/\lambda_p$ is the peak wavenumber and a is half the significant wave height, and the Benjamin–Feir index (BFI). Here the BFI is calculated as the ratio of the wave steepness k_pa to the spectral bandwidth $\Delta k/k_p \approx 2\Delta\omega/\omega_p$, where Δk and $\Delta\omega$ are measures of the width of the spectrum estimated as the half-width at the half-maximum (see Onorato *et al.* 2006 for details). The values of the input spectral parameters as well as those of the significant wave height, wave steepness and BFI are summarized in table 1. Note that the amplitude a in Socquet-Juglard *et al.* (2005) and Gramstad & Trulsen (2007) has been defined as $a = H_s/(2\sqrt{2})$. Therefore, their steepness and BFI are a factor $\sqrt{2}$ smaller than those defined here.

A $\cos^N(\vartheta)$ function is then applied to model the directional distribution of energy (see, for example, Hauser *et al.* 2005). In order to consider different degrees of the directional spreading, different values of the spreading coefficient N were used, ranging from fairly long-crested (large N) to short-crested (small N) waves. The following values were selected: $N = 840$, 200, 90, 50, 24 (see figure 2).

https://doi.org/10.1017/S002211201000385X Published online by Cambridge University Press

3. Numerical methods

3.1. *Modified nonlinear Schrödinger model*

Simulations of the random sea surface were performed using the broader bandwidth modified nonlinear Schrödinger (BMNLS) equation of Trulsen & Dysthe (1996).

NLS-type equations are usually expressed either in the complex amplitude of the surface elevation or in the complex amplitude of the velocity potential. In this work we have used the equations expressed in the non-dimensional complex amplitude of the surface elevation.

Also, NLS-type equations can be formulated in different forms suitable for describing the time evolution of a spatial field or the space evolution of a temporal field. For the main numerical results in this paper, the form suitable for the time evolution was employed. Note that the HOSM model can only be formulated in a form suitable for time evolution. However, in § 5 the relation between the spatial and temporal versions of the BMNLS equation is discussed and a comparison between the two is presented.

The exact expressions for the temporal and spatial BMNLS equations, expressed in the non-dimensional complex amplitude (B) of the surface elevation, are provided below. Note that here and in the remaining § 3.1 we have adopted a non-dimensional description where space and time are made non-dimensional with the peak wavenumber and peak frequency, respectively. The temporal and spatial BMNLS equations are given by

$$\begin{aligned} &B_t + \frac{1}{2}B_x + \frac{\mathrm{i}}{8}B_{xx} - \frac{\mathrm{i}}{4}B_{yy} + \frac{\mathrm{i}}{2}|B|^2B - \frac{1}{16}B_{xxx} + \frac{3}{8}B_{xyy} + \frac{3}{2}|B|^2B_x \\ &\quad + \frac{1}{4}B^2B_x^* + \mathrm{i}B\bar{\phi}_x - \frac{5\mathrm{i}}{128}B_{xxxx} + \frac{15\mathrm{i}}{32}B_{xxyy} - \frac{3\mathrm{i}}{32}B_{yyyy} + \frac{7}{256}B_{xxxxx} \\ &\quad - \frac{35}{64}B_{xxxyy} + \frac{21}{64}B_{xyyyy} = 0, \quad z = 0, \end{aligned} \tag{3.1a}$$

$$\begin{aligned} B_x + 2B_t + \mathrm{i}B_{tt} - \frac{\mathrm{i}}{2}B_{yy} + \mathrm{i}|B|^2B - B_{tyy} - 8|B|^2B_t - 2B^2B_t^* - 4\mathrm{i}B\bar{\phi}_t \\ + \frac{3\mathrm{i}}{2}B_{ttyy} + \frac{\mathrm{i}}{8}B_{yyyy} + 2B_{tttyy} + \frac{3}{4}B_{tyyyy} = 0, \quad z = 0, \end{aligned} \tag{3.1b}$$

respectively, where the induced mean flow potential $\bar{\phi}$ is governed by

$$\bar{\phi}_{xx} + \bar{\phi}_{yy} + \bar{\phi}_{zz} = 0, \qquad -h < z < 0, \tag{3.2a}$$

$$\bar{\phi}_z = \tfrac{1}{2}(|B|^2)_x = -(|B|^2)_t, \quad z = 0, \tag{3.2b}$$

$$\bar{\phi}_z = 0, \qquad z = -h. \tag{3.2c}$$

Here the subsctipts denote partial derivatives. When B is known from (3.1a) or (3.1b), the surface displacement and the velocity potential, including the effect of bound waves, can be found from reconstruction formulae which express bound contributions in terms of the free wave complex amplitude B. The surface elevation η can be expressed as follows:

$$\eta = \bar{\eta} + \tfrac{1}{2}\left(B\mathrm{e}^{\mathrm{i}(x-t)} + B_2\mathrm{e}^{2\mathrm{i}(x-t)} + B_3\mathrm{e}^{3\mathrm{i}(x-t)} + \cdots + \text{c.c.}\right), \tag{3.3}$$

https://doi.org/10.1017/S002211201000385X Published online by Cambridge University Press

where the bound contributions are given by

$$\bar{\eta} = \frac{1}{2}\bar{\phi}_x - \frac{1}{16}(|B|^2)_{xx} - \frac{1}{8}(|B|^2)_{yy} = -\bar{\phi}_t - \frac{1}{4}(|B|^2)_{tt} - \frac{1}{8}(|B|^2)_{yy}, \tag{3.4a}$$

$$B_2 = \frac{1}{2}B^2 - \frac{\mathrm{i}}{2}BB_x + \frac{1}{2}BB_{yy} - \frac{3}{4}B_y^2 = \frac{1}{2}B^2 + \mathrm{i}BB_t - \frac{1}{2}BB_{tt} + \frac{3}{4}BB_{yy} - \frac{3}{4}B_y^2, \tag{3.4b}$$

$$B_3 = \tfrac{3}{8}B^3. \tag{3.4c}$$

Some general remarks regarding the accuracy of this reconstruction were given by Gramstad & Trulsen (2010).

The numerical method of Lo & Mei (1987) is used to solve the BMNLS equations numerically in a two-dimensional rectangular domain with a periodic boundary condition in both horizontal directions. Additional details of the numerical method can also be found in Socquet-Juglard *et al.* (2005). Since the basic unknown B, under the narrow-band assumption, is slowly varying, the integration step used in the numerical integration can be chosen relatively large. Here, the non-dimensional integration step is set to $\Delta t = \Delta x = 2\pi/10$, corresponding to 10 integration steps per peak period in the temporal evolution and 10 steps per peak wavelength in the spatial evolution. This choice is found to give a satisfactory accuracy, and the invariant $\int |B|^2 \,\mathrm{d}\boldsymbol{x}$ is conserved within 0.3 % of the initial value in all simulations.

3.2. *Higher-order spectral model*

The evolution of the surface elevation was also modelled using the numerical integration of the potential Euler equations. Assuming the hypothesis of an irrotational, inviscid and incompressible fluid flow, the velocity potential $\phi(x, y, z, t)$ satisfies the Laplace equation everywhere in the fluid. At the bottom ($z = -\infty$), the vertical velocity is zero ($\phi_z|_{-h} = 0$). At the free surface ($z = \eta(x, y, t)$), the kinematic and dynamic boundary conditions hold (Zakharov 1968):

$$\psi_t + g\eta + \tfrac{1}{2}\left(\psi_x^2 + \psi_y^2\right) - \tfrac{1}{2}W^2\left(1 + \eta_x^2 + \eta_y^2\right) = 0, \tag{3.5}$$

$$\eta_t + \psi_x\eta_x + \psi_y\eta_y - W\left(1 + \eta_x^2 + \eta_y^2\right) = 0, \tag{3.6}$$

where $W(x, y, t) = \phi_z|_\eta$ represents the vertical velocity evaluated at the free surface and $\psi(x, y, t)$ is the potential calculated on the surface. Note that (3.5) and (3.6) include the contribution of free and bound waves. Moreover, they do not have any constraints on the spectral bandwidth unlike the modified nonlinear Schrödinger model.

Numerical simulations of (3.5) and (3.6) were performed with the HOSM proposed by Dommermuth & Yue (1987) and West *et al.* (1987). A comparison of these two approaches (Clamond *et al.* 2006) showed that the formulation proposed by Dommermuth & Yue (1987) is less consistent than that proposed by West *et al.* (1987). The latter, therefore, was applied for the present study.

The HOSM is a pseudo-spectral method which uses a series expansion in the wave slope of the vertical velocity $W(x, y, t)$ about the free surface. Here, we considered a third-order expansion so that a four-wave interaction is included (see Tanaka 2001*b*, 2007). Note that the selected order of the expansion makes the HOSM consistent with the modified nonlinear Schrödinger equation as both models describe third-order effects. The expansion is then used to evaluate the velocity potential $\psi(x, y, t)$ and the surface elevation $\eta(x, y, t)$ from (3.5) and (3.6) at each instant of time. All aliasing errors generated in the nonlinear terms are removed (West *et al.* 1987; Tanaka 2001*b*). The time integration is performed by means of a fourth-order Runge–Kutta method.

https://doi.org/10.1017/S002211201000385X Published online by Cambridge University Press

A small time step, $\Delta t = T_p/100$, is used to minimize the energy leakage. The accuracy of the computation is checked by monitoring the variation of the total energy (see e.g. Tanaka 2001*a*). Despite the fact that the energy content shows a decreasing trend throughout the simulation, its variation is negligible as the relative error in total energy does not exceed 0.4 % (this result is consistent with similar simulations performed by Tanaka 2001*a*). A concise review of the HOSM can be found in Tanaka (2001*a*).

3.3. *Initial conditions and simulations*

The aim of the numerical simulations is to estimate the statistical properties of the aforementioned laboratory-generated wave fields. Therefore, the initial spectral conditions for the numerical experiments are assumed to be identical to the conditions at the wavemaker (see § 2.2).

From the directional frequency spectrum, $E(\omega, \vartheta)$, an initial two-dimensional surface $\eta(x, y, t = 0)$ was computed using first the linear dispersion relation to convert from (ω, ϑ) to wavenumber coordinates (k_x, k_y), and then the inverse Fourier transform with random amplitude and phase approximation; periodic boundary conditions were imposed. Consistent with the laboratory experiments, the random phases were assumed to be uniformly distributed over the interval $[0, 2\pi)$, while the amplitudes were Rayleigh-distributed. The velocity potential $\psi(x, y, t = 0)$, needed for the HOSM model, was then obtained from the input surface using the linear theory.

For the simulations of the potential Euler equations (HOSM), the wave field was contained in a square domain of about 14 m with a spatial mesh of 256×256 nodes ($\Delta x = \Delta y = 0.055$ m); a larger number of nodes would require unreasonable computational time. The selected grid provides a fine resolution of the physical domain as the dominant wavelength is described by about 28 grid points. In the spectral space, it allows that the maximum wavenumber, k_{max}, corresponds to the sixth harmonic of the peak of the spectrum after the wavenumbers k affected by aliasing errors are removed; a coarse resolution of the spectral peak is obtained, however.

The resolution adopted for the HOSM is not applicable for the modified nonlinear Schrödinger model, because the HOSM resolution includes Fourier modes outside the narrow bandwidth constraint of the BMNLS equation. Therefore, consistent with the underlying narrow-band assumption, we only resolve Fourier modes inside the square corresponding to a unity bandwidth. A uniform grid of 512×512 points has been employed, which corresponds to a square domain of about 400 m for wave fields with $\lambda_p = 1.56$ m. This implies a coarser grid in the physical domain, but a much finer resolution in the spectral domain, compared to the HOSM. Note that the resolution adopted for the BMNLS is to describe the free-wave complex amplitude, B, not the surface itself. When reconstructing the surface, including higher harmonic bound waves, a resampling is performed. For the resolution explained above ($n_x \times n_y = 512 \times 512$ points to describe B), the minimum number of points that can be used to describe the full surface including third-order bound waves is 3078×1536, which corresponds to about 12 points per dominant wavelength.

The laboratory experiments provided time series at some fixed distances from the wavemaker, i.e. the boundary condition imposed at $x = 0$ and the spatial evolution of the waves along the basin. The same is the case for the numerical model based on the spatial version of the BMNLS equation. However, the HOSM and the temporal BMNLS equation provide the temporal evolution of an initial wave field imposed at $t = 0$. This fundamental difference is a potential problem when comparing the numerical results with the laboratory experiments. In the following analysis, the comparison is based on the leading-order approximation that all properties are

https://doi.org/10.1017/S002211201000385X Published online by Cambridge University Press

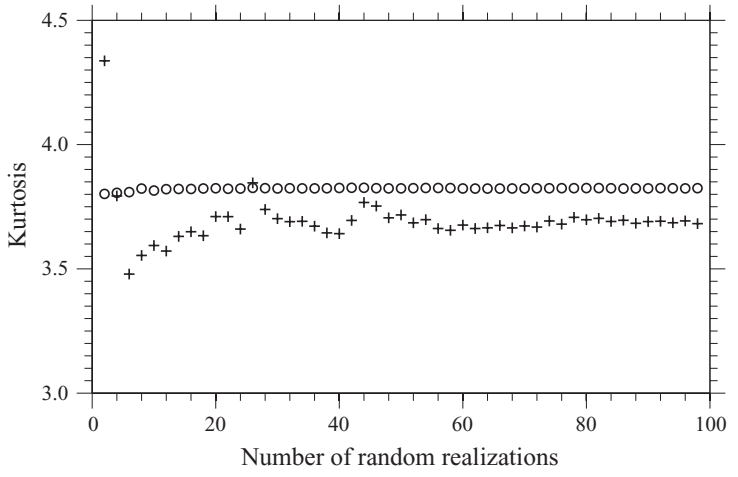


FIGURE 3. Kurtosis as a function of the number of random realizations for a directional wave field characterized by $\gamma = 6$ and $N = 840$ at $t = 24T_p$: BMNLS (○); HOSM (+).

functions of $x - c_g t$, where c_g is the group velocity of the waves. Thus, it is assumed that the location $x = \lambda_p$ in the spatial evolution corresponds to the time $t = 2T_p$ in the temporal evolution. A check on the validity of this assumption was performed by comparing the results from the spatial and temporal versions for the BMNLS model. This comparison is presented in § 5.

The total duration of the HOSM and temporal BMNLS simulations is set equal to $t = 60T_p$. The output surface elevation and velocity potential are calculated every six wave periods, i.e. at $t = 6, 12, \ldots, 54, 60T_p$. Correspondingly, using the above-mentioned approximation to relate the space and time evolution, simulations with the spatial BMNLS equation were run up to $x = 30\lambda_p$, with output every third wavelength, $x = 3, 6, \ldots, 27, 30\lambda_p$. This is also consistent with the laboratory experiments where the surface elevation was recorded up to $x \approx 30\lambda_p$. Note that modulational instability leads to deviations from normality within few peak periods or wavelengths (see e.g. Janssen 2003; Socquet-Juglard *et al.* 2005; Onorato *et al.* 2006; Annenkov & Shrira 2009). Thus, the short evolution considered in this study is sufficient to capture the formation of large-amplitude waves. Note also that the BMNLS equation may be incapable of describing some effects which take place either close to the wavemaker or soon after the start-up of the wavemaker. Because these effects are expected to decay exponentially with the distance from the wavemaker, they should not be an issue for the present study (see e.g. Shemer, Sergeeva & Slunyaev 2010).

The output surface elevation is then used to calculate the statistical properties of the wave field. About 100 realizations with the same input spectrum and different random amplitudes and phases were performed to achieve statistically significant results. We verified that the aforementioned number of realizations leads to stable estimates of the statistical moments from both models (see figure 3). In this respect, we also mention that a large number of random realizations are expected to minimize the effects related to the different sizes of the numerical domains (see e.g. Tanaka & Yokoyama 2004). The 95 % confidence intervals are smaller than ± 0.01 for the third-order moment of the p.d.f. (skewness) and ± 0.06 for the fourth-order moment (kurtosis).

https://doi.org/10.1017/S002211201000385X Published online by Cambridge University Press

4. Spectral changes

As the wave field propagates, the nonlinear interaction between wave modes generates a transfer of energy that modifies the wave spectrum (see e.g. Longuet-Higgins 1976; Onorato *et al.* 2002*b*; Dysthe *et al.* 2003). The nonlinear energy transfer is responsible for redistributing the energy such that the spectral peak is downshifted (see, for example, Hasselmann 1962; Onorato *et al.* 2002*b*). From the laboratory experiments, we observed that the peak period increased up to 3 % at $x = 15\lambda_p$, which means that the wavenumber at the spectral peak changed from 4 m^{-1} at $x = 0$ to 3.80 m^{-1} at $x = 15\lambda_p$ (additional details on the spectral downshift observed in the wave basin can be found in Onorato *et al.* 2009*a*). Approximately the same variation of the peak period was also observed from the numerical simulations of the numerical models.

A small fraction of the spectral energy is also transferred towards high wavenumbers and redistributed along two characteristic directions, forming angles of about $\pm 35.5^{\circ}$ with the mean direction of propagation (Longuet-Higgins 1976). Thus, as a result, this directional redistribution leads to the broadening of the directional spectrum towards high wavenumbers (see Dysthe *et al.* 2003; Toffoli *et al.* 2010). In order to compare the experimental and numerical results, the directional properties are summarized into a mean directional spread. An estimate of the latter can be calculated as the average over the wavenumber domain of the directional spread parameter, which, in (k, ϑ) coordinates, can be expressed as follows (see e.g. Hwang *et al.* 2000):

$$\sigma_2(k) = \left(\frac{\displaystyle\int_0^{\pi/2} \vartheta^2 \, D(k, \vartheta) \, \mathrm{d}\vartheta}{\displaystyle\int_0^{\pi/2} D(k, \vartheta) \, \mathrm{d}\vartheta} \right)^{1/2} . \tag{4.1}$$

Hereafter, the average value of $\sigma_2(k)$ over the wavenumber domain is referred to as $(\sigma_2)_m$ (note that small values of $(\sigma_2)_m$ correspond to a large value of N). In figure 4, we present a comparison between the experimental and simulated mean directional spreads at $x = 15\lambda_p$ for the experiments and at $t = 30T_p$ for both simulations (only the directional wave fields with $k_p a = 0.16$ are shown). On the whole, the numerical simulations capture the experimental mean directional spread reasonably well. However, the HOSM tends to underestimate the broadening of the directional spectrum for very long crested fields (small values of $(\sigma_2)_m$). This is not surprising because the course resolution in the Fourier space adopted for the HOSM is not enough to capture the variations of the initially narrow directional distribution.

5. Statistical properties

We now present a direct comparison between the statistical properties of the experimental and simulated directional wave fields. As mentioned, when comparing the evolution of skewness and kurtosis obtained from laboratory experiments with the numerical simulations based on time evolution, we have assumed that the evolution in time and space can be translated by applying the group velocity of the waves. To check the validity of this approximation, simulations with the spatial version of the BMNLS equation have been performed and compared with the temporal BMNLS equation. Examples of the time and space evolution of the fourth-order moment (the kurtosis) of the p.d.f., obtained using the two forms of the BMNLS equation, are shown in figure 5; lower values in figure 5 correspond to the broad directional spread, $N = 24$, while

https://doi.org/10.1017/S002211201000385X Published online by Cambridge University Press

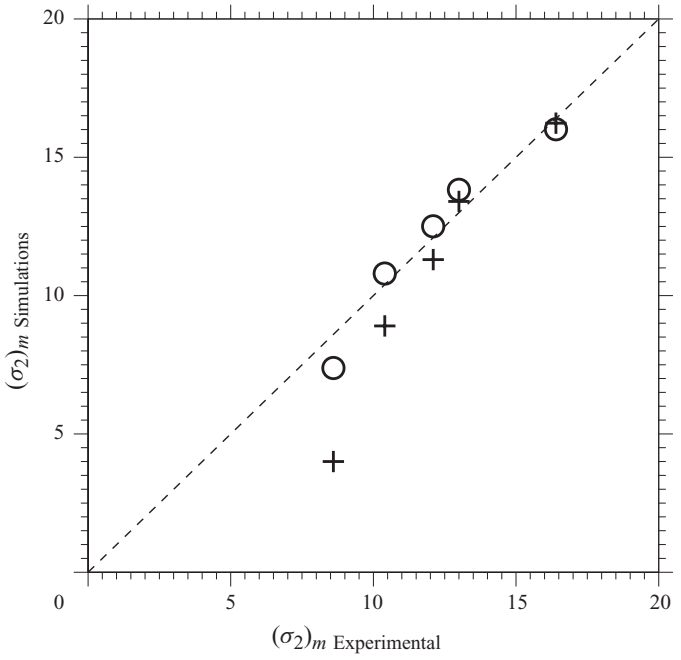


FIGURE 4. Mean directional spread at $x = 15\lambda_p$ (for experiments) and $T = 30T_p$ (for simulations). Simulations versus experimental results: BMNLS (○); HOSM (+).

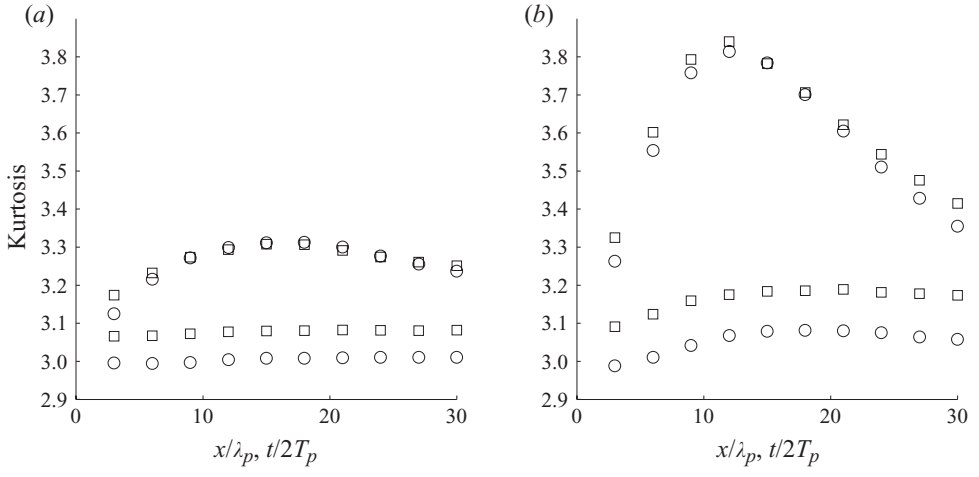


FIGURE 5. Comparison of kurtosis obtained by time (○) and space (□) integration of the BMNLS equations. Lower values correspond to the broad directional spread, $N = 24$, while greater values correspond to the narrow directional spread, $N = 840$. (*a*) $\gamma = 3$, (*b*) $\gamma = 6$.

greater values correspond to the narrow directional spread, $N = 840$. In general, the results from figure 5 show quite good agreement between the time and space evolution. For $N = 840$, we note especially that the time/point of maximum kurtosis occurs in agreement with the group-velocity transformation. For the broad directional spread, however, a somewhat higher value of the kurtosis is seen for the space evolution than for the time evolution. This may be partly explained by the fact that the

https://doi.org/10.1017/S002211201000385X Published online by Cambridge University Press

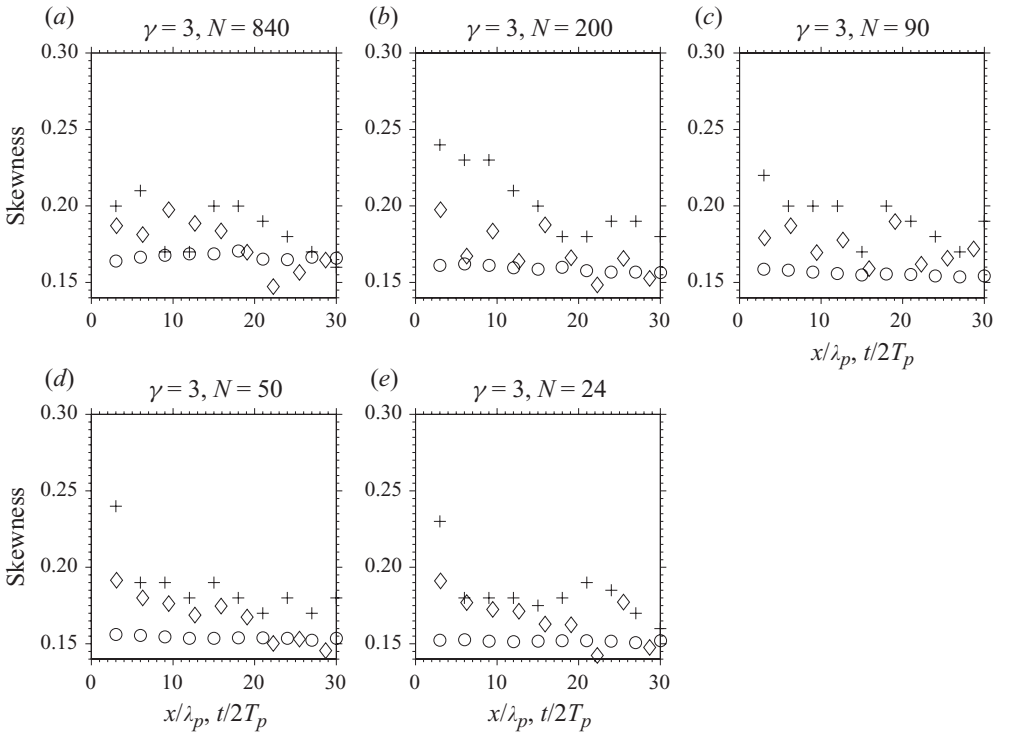


FIGURE 6. (*a–e*) Evolution of the skewness for $\gamma = 3$. Experiments ($\diamond$), BMNLS ($\circ$) and HOSM ($+$).

simulated steepness is somewhat larger for the space evolution than for the time evolution (about 6 % in the most broadband case, $\gamma = 3$, $N = 24$). This difference is due to the truncation of the spectra at unity bandwidth, since a larger part of the total energy is located outside the truncation limit in the (k_x, k_y)-spectrum than in the (ω, ϑ)-spectrum.

5.1. *Skewness and kurtosis*

In this section, we analyse the skewness and kurtosis of the surface elevation. Whereas the former describes the vertical asymmetry of the wave profile, the latter provides an indication of the occurrence of extreme events in the sample. For Gaussian processes, the skewness and kurtosis assume the values of 0 and 3, respectively. In figures 6–9, the skewness and kurtosis are presented as a function of the dimensionless distance from the wavemaker; the wavelength (λ_p) associated with the input peak period is here used as a normalizing factor.

As waves start propagating from the wavemaker, the nonlinear interaction between wave components modifies the initially symmetric profile. Waves become more vertically asymmetric with sharpening of the wave crests and the flattening of the wave troughs; as a result, the skewness departs from the Gaussian statistics. This deviation is mainly dominated by the bound modes, even though the dynamics of free waves can weakly contribute (see Onorato, Osborne & Serio 2005*a*; Mori *et al.* 2007; Toffoli *et al.* 2008*b*; Onorato *et al.* 2009*a*). Towards the end of the basin, however, the skewness shows a decreasing trend as a consequence of the spectral downshift. This reduces the steepness and hence the contribution of bound waves, which is in fact a function of the steepness (see e.g. Tayfun 1980). These features are captured by both

https://doi.org/10.1017/S002211201000385X Published online by Cambridge University Press

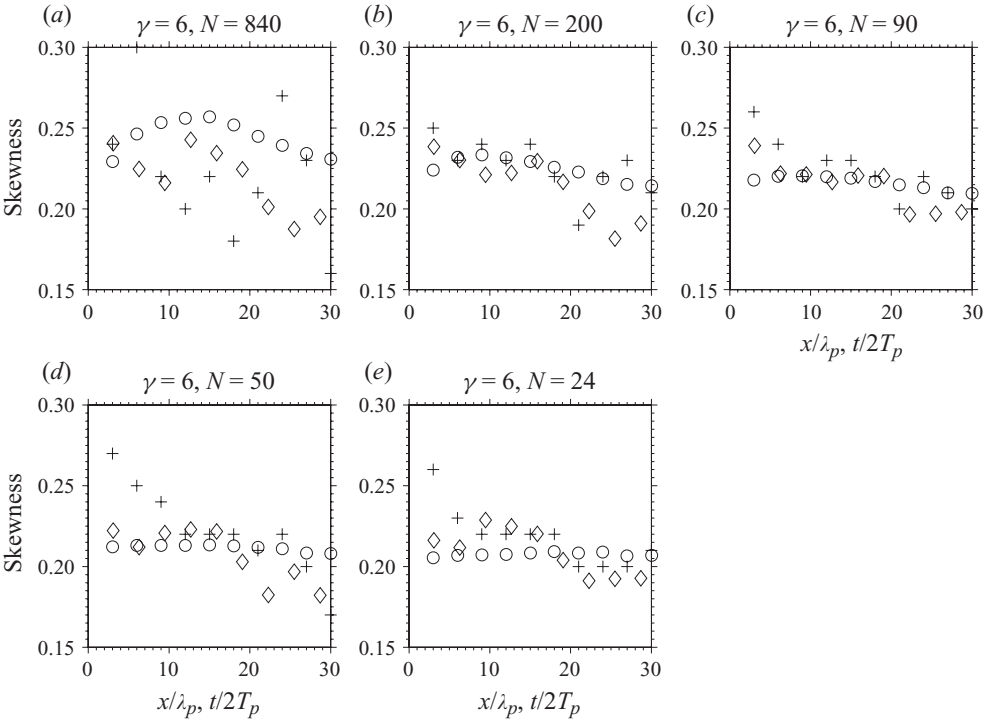


FIGURE 7. (*a–e*) Evolution of the skewness for $\gamma = 6$. Experiments (◇), BMNLS (○) and HOSM (+).

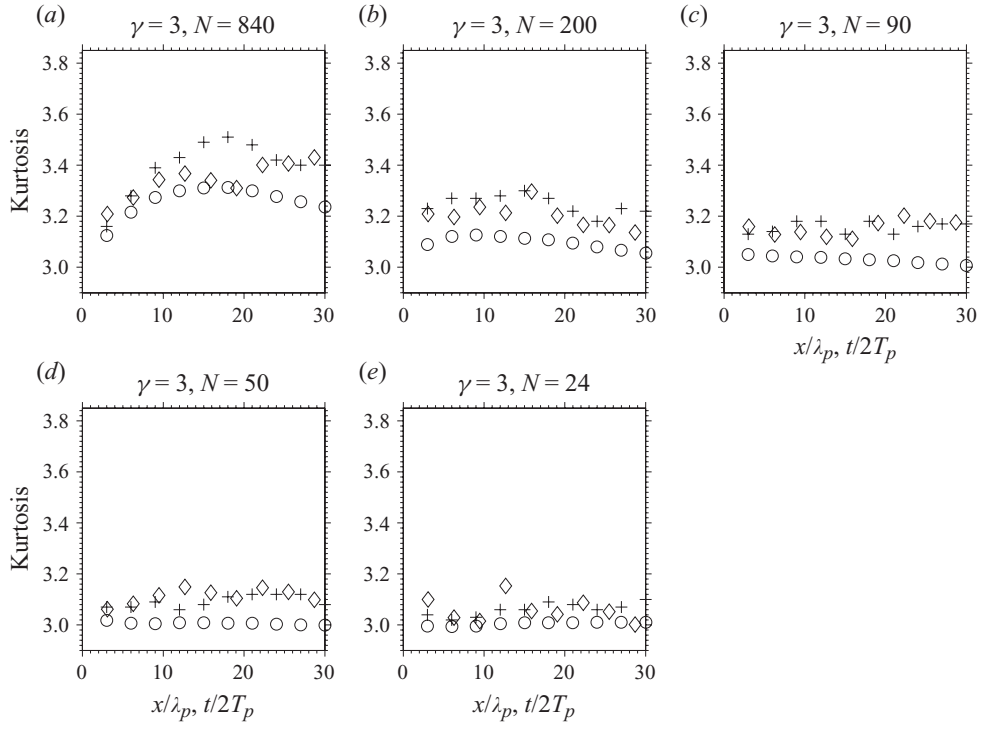


FIGURE 8. (*a–e*) Evolution of the kurtosis for $\gamma = 3$. Experiments (◇), BMNLS (○) and HOSM (+).

https://doi.org/10.1017/S002211201000385X Published online by Cambridge University Press

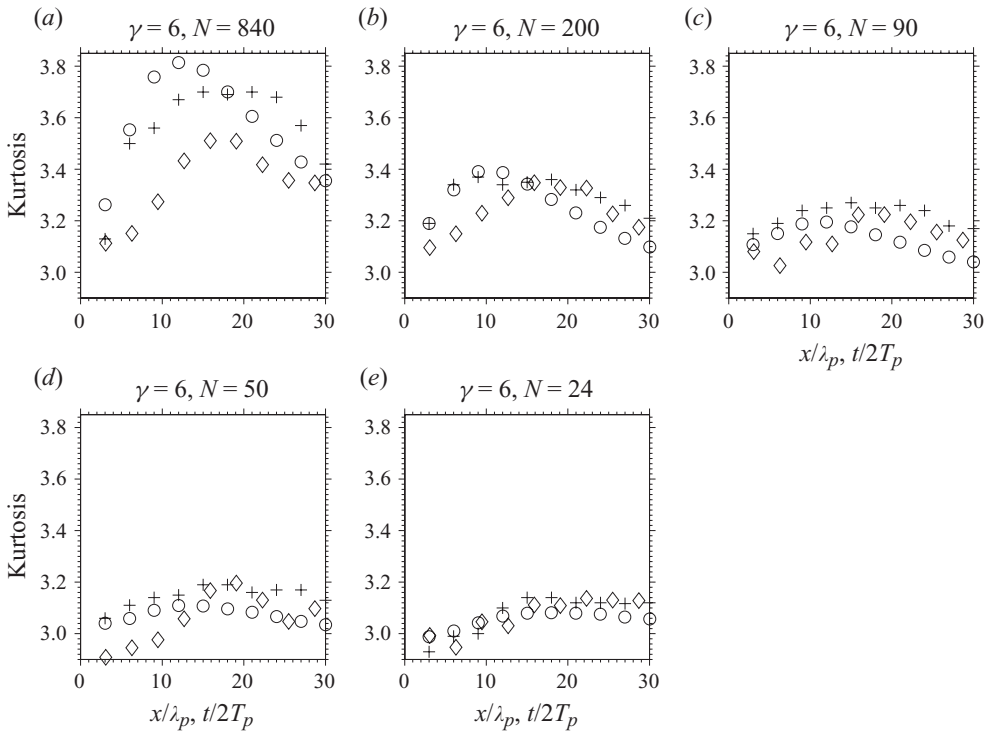


FIGURE 9. (*a–e*) Evolution of the kurtosis for $\gamma = 6$. Experiments ($\diamond$), BMNLS ($\circ$) and HOSM ($+$).

models rather well for both $k_p a = 0.13$ and 0.16. However, the numerical models seem to substantially overestimate the skewness especially for smaller steepness (differences are clearly above the confidence intervals of ± 0.01).

Because the instability of free-wavepackets to sideband perturbations gives rise to large-amplitude waves, the kurtosis can deviate substantially from normality (see e.g. Onorato *et al.* 2006). Such a deviation is well pronounced in long-crested wave fields. In our laboratory experiments, we observed that it reaches its maximum after a fairly short evolution equivalent to about 15–20 wavelengths, in agreement with previous flume experiments (Onorato *et al.* 2005*b*); the kurtosis then slowly decreases towards the end of the basin. For short-crested waves the departure from Gaussian statistics becomes less accentuated. In the case of a broad directional distribution (e.g. $N = 24$), in particular, the dynamics of free waves no longer provide a significant contribution to the statistical properties of waves and the kurtosis only weakly deviates from normality (more details can be found in Onorato *et al.* 2009*a*).

The observed dynamical evolution of mechanically generated waves is estimated reasonably well by the numerical simulations from both BMNLS and HOSM in wave fields characterized by moderate steepness ($k_p a = 0.13$ in this study, figure 8). Nonetheless, the HOSM tends to overestimate the kurtosis for very narrow directional conditions (i.e. $N = 840$). This is not surprising, though, because the spectral resolution implemented for these simulations is too coarse to capture the effects of such a narrow directional spreading (see also figure 4). The finer spectral discretization used in the BMNLS, in this respect, provides a more accurate approximation of the laboratory results. When a larger steepness is taken into account (see figure 9),

https://doi.org/10.1017/S002211201000385X Published online by Cambridge University Press

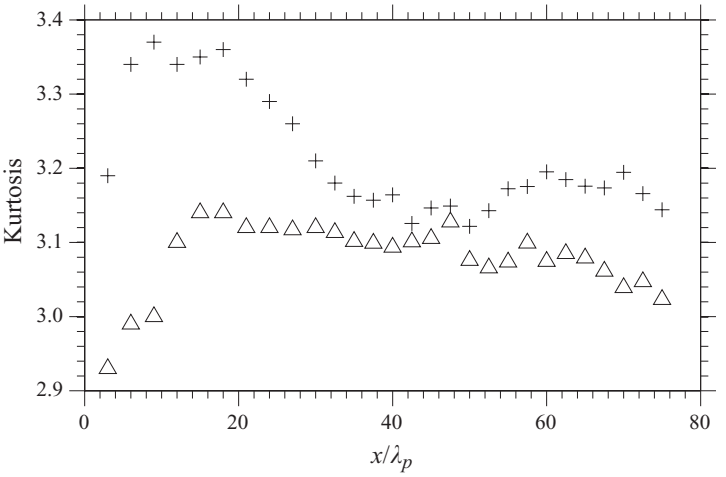


FIGURE 10. (a,b) HOSM simulation of the long-term evolution of the kurtosis. The initial wave spectrum has $\gamma = 6$, and $N = 200$ (+) and $N = 24$ (△).

however, differences between the numerical and experimental results become evident also for more short-crested conditions. Apart from the tendency to overestimate the kurtosis in wave fields with a very narrow initial directional spreading ($N = 840$), the HOSM model overpredicts the occurrence of extreme events at short fetches ($x/\lambda_p < 15$), even though the space scale for the occurrence of the maximum kurtosis is consistent with the laboratory results. Also, simulations with the BMNLS model tend to overestimate the kurtosis at short fetches. However, the BMNLS predicts the formation of an overshoot after about 10 wavelengths, which does not agree with either the HOSM model or the laboratory experiments. The prominence of this feature vanishes with increased directionality. For an initially broad directional distribution ($N = 24$), both simulations and experiments produce weak deviations from Gaussian statistics. In this respect, we mention that the HOSM and BMNLS yield the same results independently of the narrow-banded approximation of the BMNLS.

Importantly, for sufficiently steep and long-crested wave fields, the kurtosis would reach subsequent maximum values after the initial overshooting if the wave field were left free to propagate beyond $30\lambda_p$. However, the deviation from normality would be gradually attenuated owing to the downshift of the spectral peak, which reduces the wave steepness, and the broadening of the directional spreading (see figure 10). In the case of short-crested seas, the kurtosis would not show any significant deviation from normality. Thus, the short evolution period considered in this study is sufficient to address the most non-Gaussian properties of the wave field.

From a practical point of view, it is of great importance to verify the accuracy of numerical models to predict the maximum kurtosis. In figure 11, we summarize the maximum kurtosis as a function of the mean directional spread (4.1) for both models and experiments. As mentioned earlier, short-crestedness results in a substantial reduction of the effect of the modulational instability, which basically vanishes for broad directional distributions (cf. Waseda *et al.* 2009; Onorato *et al.* 2009*b*). For both of the selected wave steepnesses, the BMNLS and HOSM models provide a good qualitative and quantitative estimate for the measured maximum kurtosis and the transition from strongly to weakly non-Gaussian conditions. Note, however, that the difference between the experimental and numerical kurtosis is lower than the

https://doi.org/10.1017/S002211201000385X Published online by Cambridge University Press

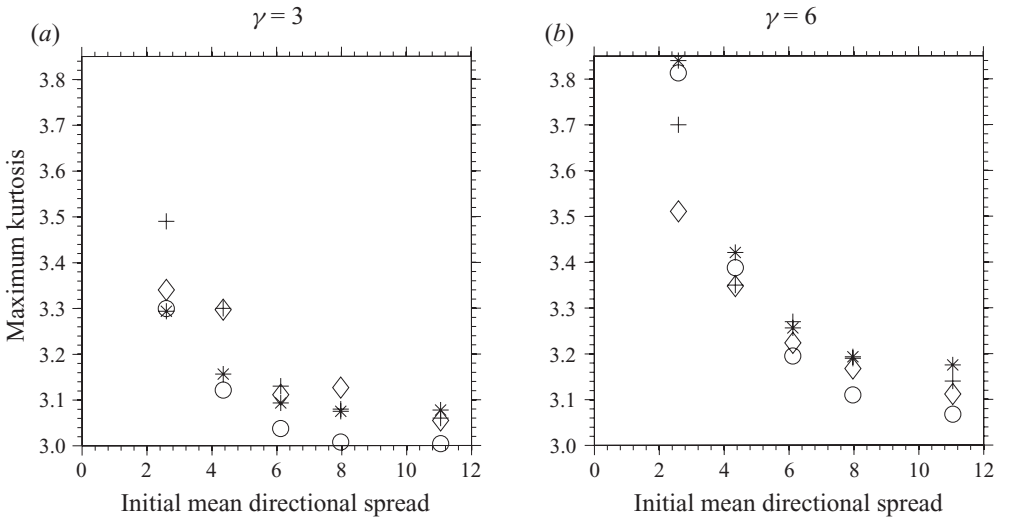


FIGURE 11. (*a, b*) Maximum kurtosis as a function of the initial directional spread. Experiments (◇), temporal BMNLS (○), spatial BMNLS (*) and HOSM (+).

statistical variability of the samples for $N \leqslant 90$ (or $(\sigma_2)_m \geqslant 6.12$), while it is slightly larger for $N \geqslant 200$ (or $(\sigma_2)_m \leqslant 4.35$). The space evolution BMNLS equation appears in most cases to give a slightly better estimate for the maximum kurtosis than the time evolution BMNLS equation. For very narrow-banded directional spectra ($N = 840$ or $(\sigma_2)_m = 2.6$), however, the models overestimate the kurtosis, especially for large steepness. This directional spreading, nonetheless, is not representative of real ocean conditions.

5.2. *Effect of discreteness on the probability of occurrence of extreme waves*

The numerical models describe the evolution of the wave fields within a finite number of grid points. In this respect, a number of studies have demonstrated that the discreteness of the computational domain can influence how waves interact (see, for example, Tanaka & Yokoyama 2004; Lvov, Nazarenko & Pokorni 2006). In terms of spectral energy, however, Tanaka & Yokoyama (2004) observed that the nonlinear energy transfer for a continuous spectrum can be reproduced regardless of the dimension of the computational mesh, provided that an ensemble average is taken over a sufficient number of random realizations (the coarser the resolution the larger the number of realizations). Nonetheless, it is not yet completely clear what is the effect of discreteness on wave statistics in general and the probability of occurrence of extreme waves in particular. In the following, we use HOSM simulations to investigate the variability of the kurtosis when the dimension of the computational domain changes.

For convenience, the number of grid points was left unaltered, i.e. 256×256 (as mentioned earlier, a larger number would require an unreasonable computational time). The computational domain was however modified by changing the grid size in the physical domain. Compared with the original computational domain, the mesh size was almost doubled ($\Delta x = \Delta y = 0.10$ m). This implies a coarser grid in the physical domain, where a dominant wavelength is now discretized by 16 grid points, and a finer resolution in the spectral space, which however occurs at the expense of high spectral components (after removal of aliasing errors, the maximum

https://doi.org/10.1017/S002211201000385X Published online by Cambridge University Press

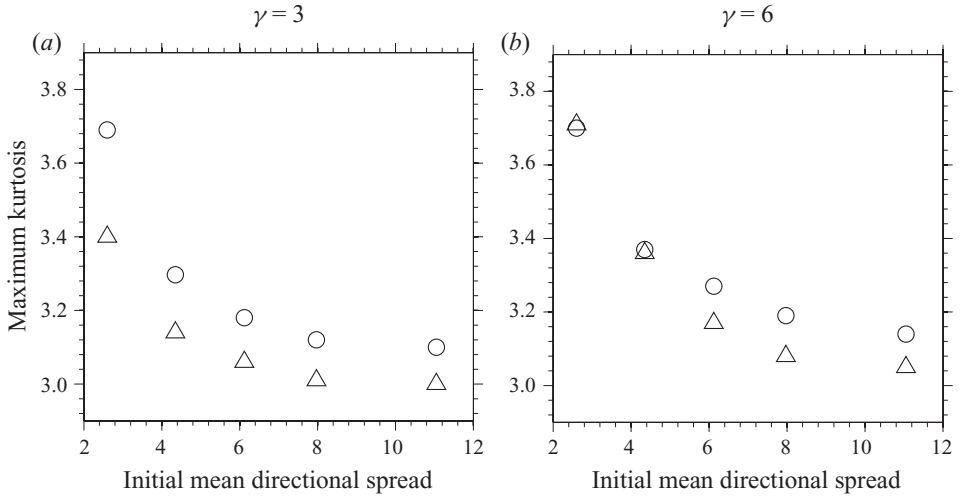


FIGURE 12. (a,b) Maximum kurtosis from HOSM simulations as a function of the initial directional spread for sea states with $\gamma = 6$: $\Delta x = \Delta y = 0.055\,\mathrm{m}$ (○); $\Delta x = \Delta y = 0.10\,\mathrm{m}$ (△).

wavenumber $k_{max} = 3k_p$). The simulations were conducted considering the same initial spectral conditions and following the same procedure described in § 3.3 (hence with the same number or random realization, i.e. 100).

In figure 12, the maximum kurtosis as computed with different computational grids is presented as a function of the initial mean directional spread. For spectral conditions with $k_p a = 0.13$ (or $\gamma = 3$), the changes in the computational domain produce a rather significant reduction of the kurtosis. On average, the kurtosis is reduced to about 4.9 %. In the case of steeper wave fields ($k_p a = 0.16$ or $\gamma = 6$), the modified computational domain does not have effects on the maximum kurtosis for long-crested wave fields ($N = 840$ and 200 or $(\sigma_2)_m = 2.6$ and 4.35), while it reduces the kurtosis to about 3.5 % for more short-crested conditions ($N \leqslant 90$ or $(\sigma_2)_m \geqslant 6.12$). Note that a finer resolution in the spectral space provides a better description of the spectral evolution also for long-crested wave fields. In this respect, after about $30T_p$, the mean directional spread for $N = 840$ and 200 is consistent with both BMNLS simulations and laboratory experiments.

Since the reduction of the maximum kurtosis may be due to both the finer grid in the spectral space and the coarser resolution of the physical domain, it is difficult to reach a firm conclusion. However, it is worth mentioning that these results are to a certain extent consistent with the simulations of the BMNLS, which are computed over a finer spectral space. For $k_p a = 0.13$, in fact, the BMNLS equation shows a systematically lower kurtosis than that computed by the HOSM. For $k_p a = 0.16$, on the other hand, the BMNLS shows a rather high kurtosis in long-crested sea states and a lower kurtosis for more short-crested wave fields (see figure 11).

5.3. *Probability density function of the surface elevation*

In figures 13 and 14, we present the p.d.f. of the surface elevation when the maximum kurtosis is recorded. For convenience, we scale the surface elevation by the concurrent standard deviation σ. The numerical and experimental p.d.f.s are compared to the Gaussian distribution and the Tayfun second-order distribution (see Tayfun 1980 and (8) in Socquet-Juglard *et al.* 2005 for details).

https://doi.org/10.1017/S002211201000385X Published online by Cambridge University Press

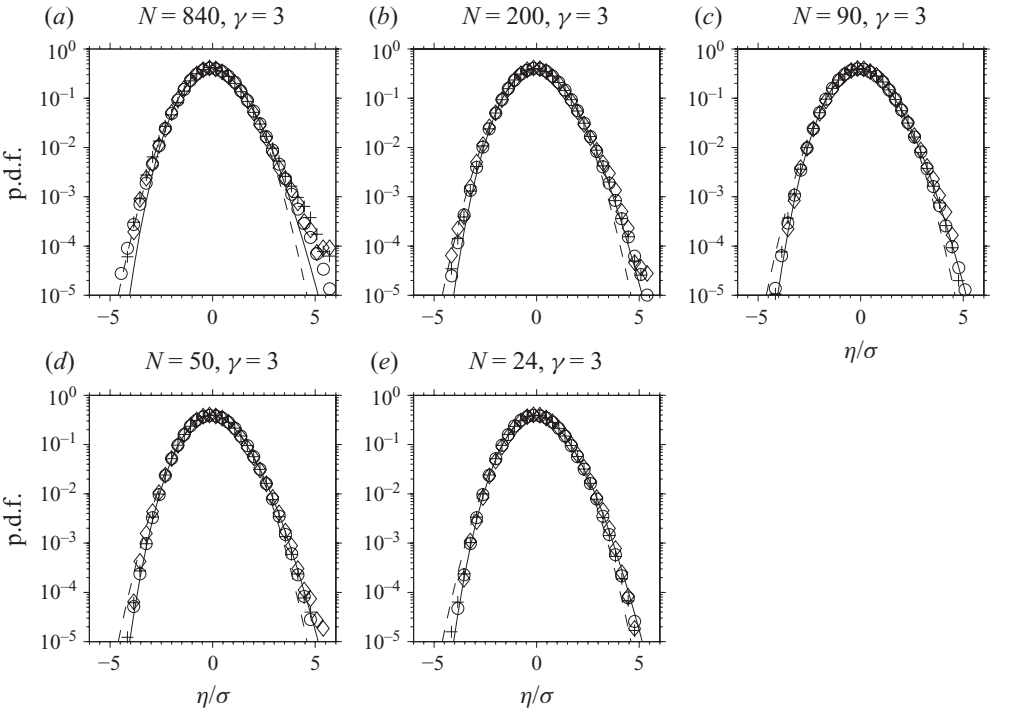


FIGURE 13. (*a–e*) The p.d.f. of the surface elevation for different directional spreading and $\gamma = 3$: experiments (◇), BMNLS (○) and HOSM (+). Normal distribution (dashed line) and the Tayfun distribution (solid line) are also displayed.

In agreement with previous experimental and numerical studies (for example Socquet-Juglard *et al.* 2005; Onorato *et al.* 2009*a*; Waseda *et al.* 2009), we observed that the p.d.f. shows a substantial deviation of both its tails from the Tayfun distribution, when the spectral energy is concentrated over a narrow range of directions (crests are higher and troughs are deeper than the second-order model predicts). Under these circumstances, in fact, the contribution of the nonlinear dynamics of free wave modes dominates the statistical properties of the wave field. Although the numerical models are not fully nonlinear, they are able to capture the aforementioned deviations reasonably well for the selected initial steepness conditions.

As short-crestedness becomes more pronounced, however, the departure from the second-order theory is significantly reduced regardless of the value of the initial steepness (see cases with an initial directional spreading characterized by $N \leqslant 90$). We did not observe any substantial deviations between the experimental and numerical p.d.f.s, which fit rather well the second-order based distribution.

6. Conclusions

Experimental and numerical records of the surface elevation were studied to verify the reliability of numerical models to predict wave statistics in directional wave fields. To accomplish this task, laboratory experiments and numerical simulations of a modified nonlinear Schrödinger equation and the potential Euler equations were used to trace the evolution of the statistical properties of an initially Gaussian surface; skewness, kurtosis and the p.d.f. of the surface elevation were investigated as

https://doi.org/10.1017/S002211201000385X Published online by Cambridge University Press

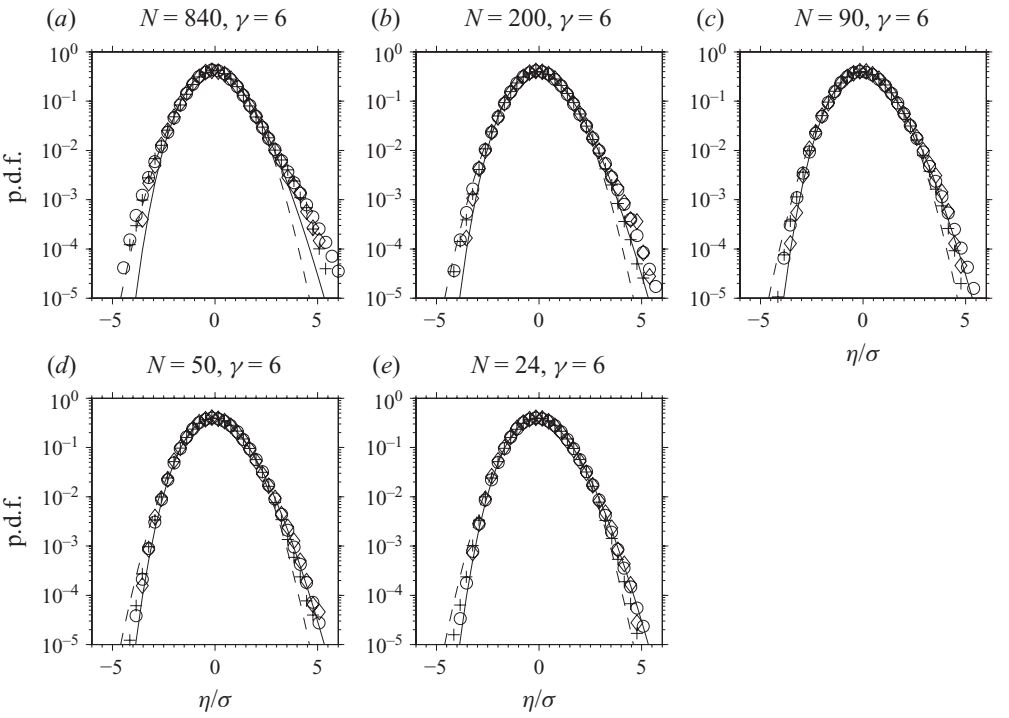


FIGURE 14. (*a–e*) The p.d.f. of the surface elevation for different directional spreading and $\gamma = 6$: experiments (◇), BMNLS (○) and HOSM (+). Normal distribution (dashed line) and the Tayfun distribution (solid line) are also displayed.

a function of the directional spreading. Note that although both models were run to describe third-order effects, the first performs under the narrow-banded assumption while the latter is free from any bandwidth constraints. Because of this constraint and the computational intensity of the potential Euler equation, a different discretization of the computational domain was implemented so that both models can run under optimal conditions. Note, however, that the discreteness of the domain introduces uncertainties of about 3–5 % in the value of the kurtosis.

The comparison between numerical and experimental results indicates that the selected models approximate the evolution of the statistical properties reasonably well. Discrepancies were encountered for a rather large initial steepness ($k_p a = 0.16$), resulting in an overestimation of the kurtosis at short distances from the wavemaker. In the case of large steepness and narrow directional spread, the modified nonlinear Schrödinger equation shows an overshoot in the evolution of the kurtosis taking place at about $t = 20T_p$ ($x \approx 10\lambda_p$). This is not consistent with either the simulations of the Euler equations or the laboratory experiments, where an overshoot, although of smaller magnitude, took place somewhat later in the evolution. It is rather surprising that the nonlinear Schrödinger model seems to perform the least well, compared to experiments, in the case of a narrow spectrum, where, in principle, it is supposed to perform the best. It is interesting to mention that the conditions at the wavemaker are produced via a linear procedure and the evolution of the wave statistics is rather sensitive to such conditions. Thus, a small deviation of the initial conditions from Gaussianity, as often observed in nature, might lead to slightly different predictions. However, this condition was considered in the present study.

https://doi.org/10.1017/S002211201000385X Published online by Cambridge University Press

From a practical point of view, nevertheless, it is essential to assert whether the models can provide a reasonable description of the maximum kurtosis as it is a measure of occurrence for extreme wave events. In this respect, our results confirm that there is good quantitative and qualitative agreement between the numerical and experimental statistics. Some discrepancies were observed for a very narrow directional distribution. We also remark that these results are based on discrete domains. Therefore, although the numerical models satisfactorily reproduce the laboratory experiments, more research is called for to achieve an accurate estimation of realistic oceanic wave fields.

It is also important to mention that both models provide similar results also for broad directional distributions despite the bandwidth constraint of the modified nonlinear Schrödinger equation.

The experimental work was supported by the European Community's Sixth Framework Programme through the grant to the budget of the Integrated Infrastructure Initiative HYDROLAB III, Contract no. 022441 (RII3). The numerical simulations with the HOSM model were partially performed by using the KU Leuven's High Performance Computing (HPC) facilities. AT has been supported by the EU project SEAMOCS (contract MRTN-CT-2005-019374). The EU project EXTREME SEAS (SCP8-GA-2009-234175) is acknowledged. A.T. also acknowledges financial support of the Australian Research Council and Woodside Energy Ltd through the grant LP0883888.

REFERENCES

Annenkov, S. Y. & Shrira, V. I. 2001 Numerical modelling of water-wave evolution based on the Zakharov equation. *J. Fluid. Mech.* **449**, 341–371.

Annenkov, S. Y. & Shrira, V. I. 2009 Evolution of kurtosis for wind waves. *Geophys. Res. Lett.* **36**, L13603.

Arhan, M. & Plaisted, R. O. 1981 Non-linear deformation of sea-wave profiles in intermediate and shallow water. *Oceanol. Acta* **4** (2), 107–115.

Bateman, W. J. D., Swan, C. & Taylor, P. H. 2001 On the efficient numerical simulation of directionally spread surface water waves. *J. Comput. Phys.* **174**, 277–305.

Benjamin, T. B. & Feir, J. E. 1967 The disintegration of wave trains on deep water. Part I: Theory. *J. Fluid Mech.* **27**, 417–430.

Bitner, E. M. (now Bitner-Gregersen, E. M.) 1980 Nonlinear effects of the statistical model of shallow-water wind waves. *Appl. Ocean Res.* **2**, 63–73.

Bitner-Gregersen, E. & Magnusson, A. K. 2004 Extreme events in field data and in a second order wave model. In *Proc. Rogue Waves 2004*, Brest, France.

Clamond, D., Francius, M., Grue, J. & Kharif, C. 2006 Long time interaction of envelope solitons and freak wave formations. *Eur. J. Mech.* B/*Fluids* **25**, 536–553.

Clamond, D. & Grue, J. 2001 A fast method for fully nonlinear water-wave computations. *J. Fluid Mech.* **447**, 337–355.

Denissenko, P., Lukaschuk, S. & Nazarenko, S. 2007 Gravity wave turbulence in a laboratory flume. *Phys. Rev. Lett.* **99**, 014501.

Dommermuth, D. G. & Yue, D. K. 1987 A high-order spectral method for the study of nonlinear gravity waves. *J. Fluid Mech.* **184**, 267–288.

Donelan, M. A., Drennan, W. M. & Magnusson, A. K. 1996 Nonstationary analysis of the directional properties of propagating waves. *J. Phys. Oceanogr.* **26**, 1901–1914.

Ducrozet, G., Bonnefoy, D., Le Touzé, D. & Ferrant, P. 2007 3-D HOS simulations of extreme waves in open seas. *Nat. Hazards Earth Syst. Sci.* **7**, 109–122.

Dysthe, K. B. 1979 Note on the modification of the nonlinear Schrödinger equation for application to deep water waves. *Proc. R. Soc. Lond.* A**369**, 105–114.

https://doi.org/10.1017/S002211201000385X Published online by Cambridge University Press

Dysthe, K., Krogstad, H. E. & Müller, P. 2008 Oceanic rogue waves. *Annu. Rev. Fluid Mech.* **40** (1), 287–310.

Dysthe, K. B., Trulsen, K., Krogstad, H. & Socquet-Juglard, H. 2003 Evolution of a narrow-band spectrum of random surface gravity waves. *J. Fluid Mech.* **478**, 1–10.

Emery, W. J. & Thomson, R. E. 2001 *Data Analysis Methods in Physical Oceanography*. Elsevier Science.

Fochesato, C. & Dias, F. 2006 A fast method for nonlinear three-dimensional free-surface waves. *Proc. R. Soc. Lond.* A **462**, 2715–2735.

Fochesato, C., Grilli, S. & Dias, F. 2007 Numerical modeling of extreme rogue waves generated by directional energy focusing. *Wave Motion* **26**, 395–416.

Forristall, G. Z. 2000 Wave crests distributions: observations and second-order theory. *J. Phys. Ocean.* **30**, 1931–1943.

Gibson, R. S., Swan, C. & Tromans, P. S. 2007 Fully nonlinear statistics of wave crest elevation calculated using a spectral response surface method: application to unidirectional sea states. *J. Phys. Ocean.* **379**, 3–15.

Gramstad, O. & Trulsen, K. 2007 Influence of crest and group length on the occurrence of freak waves. *J. Fluid Mech.* **582**, 463–472.

Gramstad, O. & Trulsen, K. 2010 Can swell increase the number of freak waves in a wind sea? *J. Fluid Mech.* **650**, 57–79.

Hasselmann, K. 1962 On the non-linear energy transfer in a gravity-wave spectrum. Part 1: General theory. *J. Fluid Mech.* **12**, 481–500.

Hauser, D., Kahma, K. K., Krogstad, H. E., Lehner, S., Monbaliu, J. & Wyatt, L. W. (Ed.) 2005 *Measuring and Analysing the Directional Spectrum of Ocean Waves*. Cost Office.

Hwang, P. A., Wang, D. W., Walsh, E. J., Krabill, W. B. & Swift, R. N. 2000 Airborne measurements of the wavenumber spectra of ocean surface waves. Part II: Directional distribution. *J. Phys. Oceanogr.* **30**, 2768–2787.

Janssen, P. A. E. M. 2003 Nonlinear four-wave interaction and freak waves. *J. Phys. Ocean.* **33** (4), 863–884.

Janssen, P. A. E. M. 2009 On some consequences of the canonical transformation in the Hamiltonian theory of water waves. *J. Fluid Mech.* **637**, 1–44.

Kharif, C. & Pelinovsky, E. 2003 Physical mechanisms of the rogue wave phenomenon. *Eur. J. Mech.* B/*Fluids* **22**, 603–634.

Komen, G. J., Cavaleri, L., Donelan, M., Hasselmann, K., Hasselmann, H. & Janssen, P. A. E. M. 1994 *Dynamics and Modelling of Ocean Waves*. Cambridge University Press.

Lo, E. Y. & Mei, C. C. 1987 Slow evolution of nonlinear deep-water waves in two horizontal directions: a numerical study. *Wave Motion* **9**, 245–259.

Longuet-Higgins, M. S. 1963 The effect of non-linearities on statistical distribution in the theory of sea waves. *J. Fluid Mech.* **17**, 459–480.

Longuet-Higgins, M. S. 1976 On the nonlinear transfer of energy in the peak of a gravity-wave spectrum: a simplified model. *Proc. R. Soc. Lond.* A **347**, 311–328.

Lvov, Y. V., Nazarenko, S. & Pokorni, B. 2006 Discreteness and its effect on water-wave turbulence. *Physica* D **218**, 24–35.

Mori, N., Onorato, M., Janssen, P. A. E. M., Osborne, A. R. & Serio, M. 2007 On the extreme statistics of long-crested deep water waves: theory and experiments. *J. Geophys. Res.* **112**, C09011.

Mori, N. & Yasuda, T. 2002 Effects of high-order nonlinear interactions on unidirectional wave trains. *Ocean Engng* **29**, 1233–1245.

Onorato, M., Cavaleri, L., Fouques, S., Gramstad, O., Janssen, P. A. E. M., Monbaliu, J., Osborne, A. R., Pakozdi, C., Serio, M., Stansberg, C. T., Toffoli, A. & Trulsen, K. 2009*a* Statistical properties of mechanically generated surface gravity waves: a laboratory experiment in a three-dimensional wave basin. *J. Fluid Mech.* **627**, 235–257.

Onorato, M., Osborne, A. R. & Serio, M. 2002*a* Extreme wave events in directional random oceanic sea states. *Phys. Fluids* **14** (4), 25–28.

Onorato, M., Osborne, A. R. & Serio, M. 2005*a* On deviations from Gaussian statistics for surface gravity waves. In *Rogue Waves: Proceedings of the Hawaiian Winter Workshop*. University of Hawaii at Manoa, pp. 79–83.

https://doi.org/10.1017/S002211201000385X Published online by Cambridge University Press

Onorato, M., Osborne, A. R., Serio, M. & Bertone, S. 2001 Freak waves in random oceanic sea states. *Phys. Rev. Lett.* **86** (25), 5831–5834.

Onorato, M., Osborne, A. R., Serio, M. & Cavaleri, L. 2005*b* Modulational instability and non-Gaussian statistics in experimental random water-wave trains. *Phys. Fluids* **17**, 078101.

Onorato, M., Osborne, A., Serio, M., Cavaleri, L., Brandini, C. & Stansberg, C. T. 2006 Extreme waves, modulational instability and second order theory: wave flume experiments on irregular waves. *Eur. J. Mech.* B/*Fluids* **25**, 586–601.

Onorato, M., Osborne, A. R., Serio, M., Resio, D., Puskarev, A., Zakharov, V. E. & Brandini, C 2002*b* Freely decaying weak turbulence for sea surface gravity waves. *Phys. Rev. Lett.* **89**, 144501.

Onorato, M., Waseda, T., Toffoli, A., Cavaleri, L., Gramdstad, O., Janssen, P. A. E. M., Kinoshita T., Monbaliu, J., Mori, N., Osborne, A. R., Serio, M., Stansberg, C. T., Tamura, H. & Trulsen, K. 2009*b* Statistical properties of directional ocean waves: the role of the modulational instability in the formation of extreme events. *Phys. Rev. Lett.* **102**, 114502.

Petrova, P, Cherneva, Z. & Guedes Soares, C. 2006 Distribution of crest heights in sea states with abnormal waves. *Appl. Ocean Res.* **28**, 235–245.

Prevosto, M., Krogstad, H. E. & Robin, A. 2000 Probability distributions for maximum wave and crest heights. *Coast. Engng* **40**, 329–360.

Shemer, L., Sergeeva, A. & Slunyaev, A. 2010 Applicability of envelope model equations for simulation of narrow-spectrum unidirectional random wave field evolution: experimental validation. *Phys. Fluids* **22**, 016601.

Socquet-Juglard, H., Dysthe, K., Trulsen, K., Krogstad, H. E. & Liu, J. 2005 Distribution of surface gravity waves during spectral changes. *J. Fluid Mech.* **542**, 195–216.

Stansberg, C. T. 1994 Effects from directionality and spectral bandwidth on non-linear spatial modulations of deep-water surface gravity waves. In *Proceedings of the 24th International Conference on Coastal Engineering, Kobe, Japan*, vol. 1, pp. 579–593.

Tanaka, M. 2001*a* A method of studying nonlinear random field of surface gravity waves by direct numerical simulations. *Fluid Dyn. Res.* **28**, 41–60.

Tanaka, M. 2001*b* Verification of Hasselmann's energy transfer among surface gravity waves by direct numerical simulations of primitive equations. *J. Fluid Mech.* **444**, 199–221.

Tanaka, M. 2007 On the role of resonant interactions in the short-term evolution of deep-water ocean spectra. *J. Phys. Ocean.* **37**, 1022–1036.

Tanaka, M. & Yokoyama, N. 2004 Effects of discretization of the spectrum in water-wave turbulence. *Fluid Dyn. Res.* **34**, 199–216.

Tayfun, M. A. 1980 Narrow-band nonlinear sea waves. *J. Geophys. Res.* **85** (C3), 1548–1552.

Tayfun, M. A. & Fedele, F. 2007 Wave-height distributions and nonlinear effects. *Ocean Engng* **34**, 1631–1649.

Toffoli, A., Benoit, M., Onorato, M. & Bitner-Gregersen, E. M. 2009 The effect of third-order nonlinearity on statistical properties of ransom directional waves in finite depth. *Nonlin. Process. Geophys.* **16**, 131–139.

Toffoli, A., Bitner-Gregersen, E., Onorato, M. & Babanin, A. V. 2008*a* Wave crest and trough distributions in a broad-banded directional wave field. *Ocean Engng* **35**, 1784–1792.

Toffoli, A., Onorato, M., Babanin, A. V., Bitner-Gregersen, E., Osborne, A. R. & Monbaliu, J. 2007 Second-order theory and set-up in surface gravity waves: a comparison with experimental data. *J. Phys. Ocean.* **37**, 2726–2739.

Toffoli, A., Onorato, M., Bitner-Gregersen, E., Osborne, A. R. & Babanin, A. V. 2008*b* Surface gravity waves from direct numerical simulations of the Euler equations: a comparison with second-order theory. *Ocean Engng* **35** (3–4), 367–379.

Toffoli, A., Onorato, M., Bitner-Gregersen, E. M. & Monbaliu, J. 2010 The development of a bimodal structure in ocean wave spectra. *J. Geophys. Res.* **115**, C03006.

Trulsen, K. & Dysthe, K. B. 1996 A modified nonlinear Schrödinger equation for broader bandwidth gravity waves on deep water. *Wave Motion* **24**, 281–289.

Tsai, W.-T. & Yue, D. K. 1996 Computation of nonlinear free-surface flows. *Annu. Rev. Fluid Mech.* **28**, 249–278.

Waseda, T., Kinoshita, T. & Tamura, H. 2009 Evolution of a random directional wave and freak wave occurrence. *J. Phys. Oceanogr.* **39**, 621–639.

https://doi.org/10.1017/S002211201000385X Published online by Cambridge University Press

West, B. J., Brueckner, K. A., Jand, R. S., Milder, D. M. & Milton, R. L. 1987 A new method for surface hydrodynamics. *J. Geophys. Res.* **92** (C11), 11803–11824.

Young, I. R. 1994 On the measurement of directional wave spectra. *Appl. Ocean Res.* **16**, 283–294.

Zakharov, V. 1968 Stability of period waves of finite amplitude on surface of a deep fluid. *J. Appl. Mech. Tech. Phys.* **9**, 190–194.

Zakharov, V. E., Dyachenko, A. I. & Vasilyev, O. A. 2002 New method for numerical simulation of a nonstationary potential flow of incompressible fluid with a free surface. *Eur. J. Mech.* B/*Fluids* **21**, 283–291.

Zakharov, V. E. & Shabat, P. B. 1972 Exact theory of two-dimensional self-focusing and one-dimensional self-modulation of waves in nonlinear media. *Sov. Phys. JETP* **34**, 62–69.

https://doi.org/10.1017/S002211201000385X Published online by Cambridge University Press